

www.acsami.org Research Article

# Bond Switching in Densified Oxide Glass Enables Record-High Fracture Toughness

Theany To, Søren S. Sørensen, Johan F. S. Christensen, Rasmus Christensen, Lars R. Jensen, Michal Bockowski, Mathieu Bauchy, and Morten M. Smedskjaer\*



Cite This: ACS Appl. Mater. Interfaces 2021, 13, 17753-17765



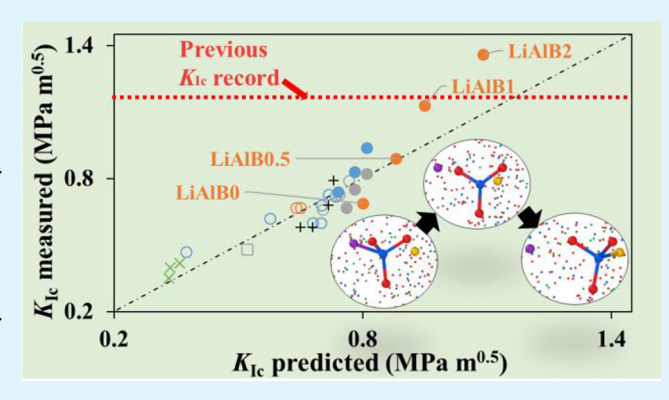
**ACCESS** 

III Metrics & More

Article Recommendations

s Supporting Information

ABSTRACT: Humans primarily interact with information technology through glass touch screens, and the world would indeed be unrecognizable without glass. However, the low toughness of oxide glasses continues to be their Achilles heel, limiting both future applications and the possibility to make thinner, more environmentally friendly glasses. Here, we show that with proper control of plasticity mechanisms, record-high values of fracture toughness for transparent bulk oxide glasses can be achieved. Through proper combination of gas-mediated permanent densification and rational composition design, we increase the glasses' propensity for plastic deformation. Specifically, we demonstrate a fracture toughness of an aluminoborate glass (1.4 MPa m<sup>0.5</sup>) that is twice as high as that of commercial glasses for mobile devices. Atomistic simulations



reveal that the densification of the adaptive aluminoborate network increases coordination number changes and bond swapping, ultimately enhancing plasticity and toughness upon fracture. Our findings thus provide general insights into the intrinsic toughening mechanisms of oxide glasses.

KEYWORDS: bond switching, oxide glasses, fracture toughness, toughening mechanism, molecular dynamics

# 1. INTRODUCTION

To limit raw material usage and preparation footprint, development of strong and tough materials is of paramount importance for advanced structural applications.<sup>1,2</sup> However, the apparent conflict between the strength and toughness of materials poses a significant challenge.<sup>3,4</sup> For example, metals exhibit dislocation movement under stress, resulting in high fracture toughness and low yield strength. Glasses, particularly oxide glasses with ionic-covalent bonding, are generally unlikely to yield plastically under an opening stress, resulting in low fracture toughness and, theoretically, in high yield strength. Oxide glasses generally feature transparency, high hardness, easy formability, and relatively low cost, and as such, they are used in many sectors, including electronics, photonics, informatics, and infrastructure. In certain amorphous oxides, it has been possible to improve properties such as strength and toughness, enabling advanced applications within optoelectronics,<sup>5</sup> flexible electronics,<sup>6</sup> and battery technologies.<sup>7</sup> The experimental strength of oxide glasses, as well as other brittle materials, is much lower than the theoretical one due to stress concentration on the flaws generated during processing and/or handing. While it is possible to design glass compositions with high resistance to surface defect formation, 8,9 completely prohibiting the occurrence of such flaws appears impossible. Moreover, the typical post-treatment methods such as thermal

tempering and ion exchange mainly increase strength <sup>10,11</sup> but not the internal resistance to crack growth (i.e., fracture toughness <sup>12</sup>). As such, it is desirable to design glasses with improved resistance to the growth of these inevitable flaws through intrinsic toughening mechanisms. Such strong and tough glasses would enable thinner, more environmentally friendly glass products from window panels and car windshields to touch screens and bioactive glasses. They would also improve safety and reduce injuries arising from glass fracture, e.g., during car crashes.

Currently, the fracture toughnesses of all commercially available oxide glasses are reported to be lower than 1 MPa  $\rm m^{0.5}$ ,  $\rm l^{3-1.5}$  as measured using self-consistent methods (e.g., the three methods in the ASTM standard  $\rm l^{16}$ ). There is thus a need to understand the underlying mechanisms of intrinsic toughening to enable the design of tougher oxide glasses. To our knowledge, the highest experimentally measured fracture toughness is of a bulk aluminosilicate glass (1.17 MPa  $\rm m^{0.5}$ )

Received: January 8, 2021 Accepted: March 24, 2021 Published: April 6, 2021





using the short chevron notched beam method.<sup>17</sup> A sodium silicate glass simulated by molecular dynamics (MD) showed a higher value of 1.25 MPa m<sup>0.5</sup> when pressure-quenched from 22 GPa. 18 The authors proposed that such high toughness could be ascribed to the pressure-induced increase in rigidity and crack tip blunting leading to stress relaxation. Another recent study on simulated densified silica glass showed a somewhat similar increase in nanoductility upon compression, owing to the decreasing coordination number of Si atoms during loading.<sup>19</sup> In studies on nanoscale samples, higher values of toughness have been reported for amorphous oxides based on their high degree of ductility under compressive/tensile stress. 20-22 For example, in nanoscale amorphous silica, ductility originates from silicon atoms with stress-induced exchange of bonded oxygen atoms with other SiO<sub>4</sub> groups while remaining in the same coordination state. 20,21 Here, we will define such events as "bond swapping" events. Similarly, in nanoscale amorphous alumina, the observed ductility is ascribed to the increase in the aluminum coordination number from four to six as well as from swapping of oxygens under a high strain rate.<sup>22</sup>

Here, we demonstrate how control of the plasticity mechanism and enhanced bond switching (i.e., swapping, increasing, and decreasing coordination number) induced by pressure densification can be used to tailor the macroscale fracture response of oxide glasses. Specifically, we prepare three different glass compositions (13Na<sub>2</sub>O-6MgO-10CaO-71SiO<sub>2</sub> (commercial window glass), 25Li<sub>2</sub>O-20Al<sub>2</sub>O<sub>3</sub>-55B<sub>2</sub>O<sub>3</sub>, and 35Na<sub>2</sub>O-20B<sub>2</sub>O<sub>3</sub>-45SiO<sub>2</sub>) with both similar Young's modulus (~70 GPa) and fracture toughness (~0.7 MPa  $\dot{m}^{0.5}$ ). Upon subjection to isostatic N<sub>2</sub>-mediated high-temperature pressure treatment, the measured change in their fracture toughness (determined by the single-edge precracked beam (SEPB) method<sup>16,23</sup>) is highly composition-dependent. The densified aluminoborate glass exhibits a record-high fracture toughness  $(1.36~\mathrm{MPa~m}^{0.5})$ . We clarify the atomistic origin of this unprecedented fracture toughness based on MD simulations and theoretical predictions, ultimately leading to a set of new structural design principles for achieving transparent yet ultratough bulk oxide glasses.

#### 2. METHODS

2.1. Experimental Sample Preparation. In this study, we used three different oxide glass compositions (in mol %), namely, 13Na<sub>2</sub>O-6MgO-10CaO-71SiO<sub>2</sub> (SLS), 25LiO<sub>2</sub>-20Al<sub>2</sub>O<sub>3</sub>-55B<sub>2</sub>O<sub>3</sub> (LiAlB), and 35Na<sub>2</sub>O-20B<sub>2</sub>O<sub>3</sub>-45SiO<sub>2</sub> (NaBSi). The studied glasses have a similar fracture toughness ( $K_{\rm Ic}$ ) of ~0.7 MPa m<sup>0.5</sup>, similar Young's modulus (E) of ~70 GPa, and Poisson's ratios ( $\nu$ ) of 0.24, 0.26, and 0.28 for SLS, LiAlB, and NaBSi, respectively. SLS, LiAlB, and NaBSi have glass transition temperatures ( $T_{\rm g}$ ) of 560, 477, and 462 °C, respectively. The soda-lime-silica (window) glass was obtained from VELUX A/S, while the lithium aluminoborate and sodium borosilicate glasses were prepared by the traditional melt-quenching technique. We used Li<sub>2</sub>CO<sub>3</sub> (Sigma Aldrich, >99.9%), Al<sub>2</sub>O<sub>3</sub> (Sigma Aldrich, >99.5%), H<sub>3</sub>BO<sub>3</sub> (Honeywell, >99.5%), SiO<sub>2</sub> (Sigma Aldrich, >99.5%), and Na<sub>2</sub>CO<sub>3</sub> (Honeywell, >99.5%) powders. These were weighed in adequate amounts and mixed to yield ~120 g batches. The mixture was melted in a Pt-Rh crucible at 1400 °C for ~2 h in an electric furnace (Entech, Ängelholm, Sweden), and then the melt was quenched onto a brass plate. The weight loss during melting was less than ~3% for both LiAlB and NaBSi. The obtained samples were annealed at their measured  $T_{\rm g}$  for ~30 min.

After cooling down to room temperature, each glass, including the SLS glass, was carefully cut into beams of dimensions  $3\times4\times25~\text{mm}^3$  for use in the standard SEPB method <sup>16,25</sup> by using a diamond disk

(thickness of 0.4 mm) and of  $2 \times 3 \times 10$  mm³ for the adapted SEPB method² by using a thin diamond disk (thickness of 0.15 mm). We used the standard SEPB method for as-prepared, 0.5 GPa compressed, and 1 GPa compressed glasses as these may be prepared in adequate sizes for the standard setup. However, for the 2 GPa compressed glasses, the dimensions of the hot-compression chamber only allow pressure treatments of rather small samples ( $5 \times 5 \times 10$  mm³); thus, an adapted SEPB setup was used as described previously. To cut the glasses, we used the rotation and translation speeds of 1600 rpm and 0.05 mm s¹, respectively. The samples were then ground and polished on the four edges of the specimen to have a final dimension of about  $3 \times 4 \times 25$  and  $1.4 \times 1.9 \times 10$  mm³ for standard and adapted SEPB methods, respectively. The polishing was finished with a SiC-paper with fine roughness ( $\sim 9 \ \mu m$ ) in ethanol.

The polished beam specimens were subjected to an isostatic N<sub>2</sub>mediated pressure treatment at 1 and 2 GPa for soda-lime-silica and sodium borosilicate and at 0.5, 1, and 2 GPa for lithium aluminoborate. The treatment method is described in detail elsewhere.<sup>27</sup> Four to six specimens of each glass were placed in an alumina crucible inside the furnace, which in turn is positioned inside the high-pressure chamber. The specimens were heated at a constant rate of 60 K min<sup>-1</sup> until reaching the glass transition temperature  $(T_{g})$ . We kept these conditions under the desired pressure (0.5, 1, or 2 GPa) for 60 min before cooling down to room temperature (~20 °C) at a rate of 60 K min<sup>-1</sup>. At room temperature, the pressure was relieved at a rate of 30 MPa min<sup>-1</sup>. Before further experiments, the specimens were polished with a fine SiC-paper ( $\sim$ 9  $\mu$ m roughness). All glasses were subjected to powder X-ray diffraction analysis (see Section 2.5) and were found to be fully X-ray amorphous (Figure S1 in the Supporting Information).

**2.2. Experimental Elastic Properties and Hardness.** The Young's modulus (E) and Poisson's ratio  $(\nu)$  were measured by means of ultrasonic echography. Sound waves generated by 10 MHz piezoelectric transducers were used to estimate the velocities of longitudinal  $(V_{\rm L})$  and transverse  $(V_{\rm T})$  waves by using a pulse-echo method. Using the density  $(\rho)$ , measured by means of Archimedes' method in pure ethanol  $(\geq 99.99\%)$  at room temperature  $(22\ ^{\circ}{\rm C})$ , E and  $\nu$  were then obtained by means of the following relations:

$$E = \rho \frac{3V_{\rm L}^2 - 4V_{\rm T}^2}{\left(\frac{V_{\rm L}}{V_{\rm T}}\right)^2 - 1} \tag{1}$$

$$\nu = \frac{E}{2\rho V_{\rm T}^2} - 1\tag{2}$$

Vickers hardness  $(H_{\rm V})$  was measured by means of Vickers microindentation (Duramin 5, Struers), with indents produced with a load  $(P^{\rm ind})$  of 9.81 N and a dwell time of 15 s in an ambient atmosphere (22 °C and RH ~60%). Using an optical microscope (Olympus) with a 20× magnification, we measured the two diagonal lengths of the imprint, and the average value (d) was used to calculate  $H_{\rm V}$  as follows:

$$H_{\rm V} = \frac{1.8544P^{\rm ind}}{d^2} \tag{3}$$

**2.3. Experimental Fracture Toughness and Energy.** For the 2 GPa compressed glasses, fracture toughness ( $K_{\rm Ic}$ ) was determined by means of the SEPB method adapted for the small-dimension specimen ( $1.4 \times 1.9 \times 10 \ {\rm mm}^3$ ), which has been introduced elsewhere, <sup>14</sup> following the experimental procedure given in the ASTM standard for ceramics <sup>16</sup> and the recent literature for glasses. <sup>25,28,29</sup> For the other specimens, we used the standard method for ceramics by modifying for glasses <sup>16,25</sup> to measure the toughness. To verify the reliability of the adapted SEPB setup, we have also measured the  $K_{\rm Ic}$ s of small-sized samples of all as-made samples. We find that the values measured using the adapted SEPB method are similar (within the error range) to those obtained using the standard SEPB setup (see Table S1 in the Supporting Information). This thus confirms that we can use the adapted SEPB setup to measure the toughness of the small compressed glass samples.

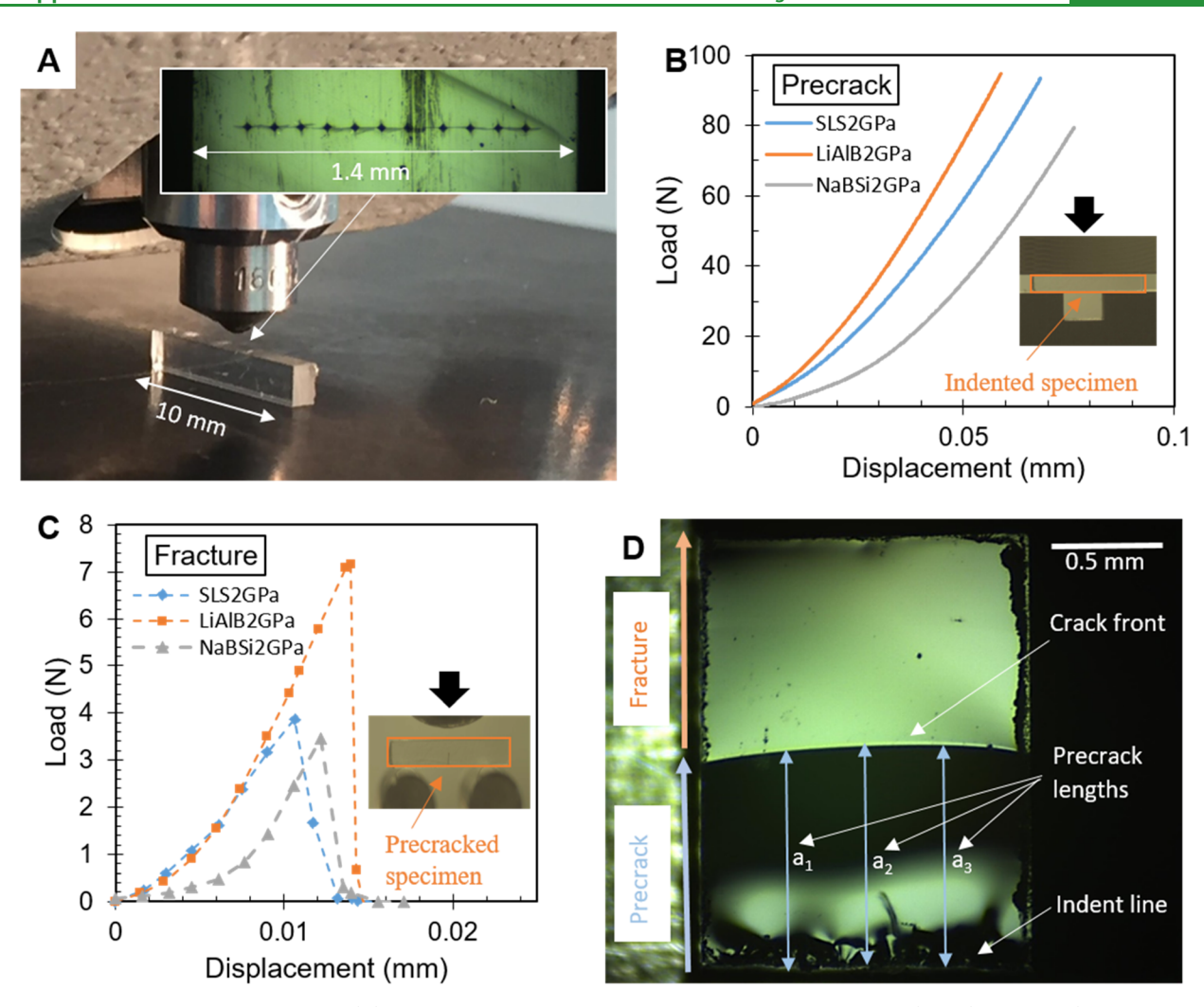


Figure 1. Fracture toughness measurement. (A) Example of indentation on the single-edge precracked beam (SEPB) specimen (2 GPa compressed lithium aluminoborate, LiAlB2GPa) with dimensions of  $1.4 \times 1.9 \times 10 \text{ mm}^3$ . The indentation line is shown in the inset. (B) Load—displacement curves of 2 GPa compressed soda-lime-silica (SLS2GPa, blue), lithium aluminoborate (LiAlB2GPa, orange), and sodium borosilicate (NaBSi2GPa, gray) glasses. The inset shows the bridge-compression fixture (groove size of 4 mm) for LiAlB2GPa as captured during precracking. (C) Load—displacement curves of three-point bending of the precracked SEPB specimens of SLS2GPa, LiAlB2GPa, and NaBSi2GPa. The three-point bending fixture with the LiAlB2GPa precracked specimen is shown in the inset. (D) Post-fractured SEPB specimen. The same LiAlB2GPa specimen is used in all images of Figure 1.

In both SEPB approaches, we introduced a line of Vickers indents (100  $\mu$ m from one indent to another) with a load of 9.81 N for a dwell time of 5 s on the broadness surface (B = 1.4 and 3 mm for adapted and standard methods, respectively). Figure 1A shows an indented specimen of 2 GPa compressed lithium aluminoborate glass. The indented specimen was positioned in the bridge-compression fixture as shown in the inset of Figure 1B. The groove sizes of 4 and 6 mm were used for adapted and standard methods, respectively, to produce a precrack using a cross-head speed of 0.05 mm min<sup>-1</sup> for both methods. When positioning the specimen into this bridgecompressive fixture (Figure 1B inset), we made sure that the indentation line was in the middle of the groove (gap as seen in Figure 1B inset). Under the bridge-compressive fixture, the specimen experiences tensile stress in the groove part and compressive stress in the other part. The tensile stress opens up the crack from the indentation line, and the crack propagates until it reaches the compressive stress, which stops the propagation. With this process, we obtain a precrack with the size about half-length of the width (W). A three-point bending fixture was used to fracture the specimen with a cross-head speed of 15  $\mu$ m s<sup>-1</sup> immediately following the precracking procedure to avoid any humidity effects (see To et al.<sup>25</sup> for details). The precrack length of the fractured specimen was measured by means of the 200× magnification microscope, as shown in Figure 1D.

The precrack front is visible, and the precrack length (a) was averaged from three lengths measured at 25, 50, and 75% (Figure 1D).  $K_{\rm Ic}$  was then calculated from the peak load ( $P_{\rm max}$ )  $^{16,25,30}$ 

$$K_{\rm Ic} = \frac{P_{\rm max}}{B\sqrt{W}}Y^* \tag{4}$$

where  $Y^*$  is defined by

$$Y^* = \frac{3}{2} \frac{S}{W} \frac{\alpha^{1/2}}{(1-\alpha)^{3/2}} f(\alpha)$$
 (5)

Here,  $\alpha$  is the precrack-width ratio (a/W) and  $f(\alpha) = [1.99 - (\alpha - \alpha^2)(2.15 - 3.93\alpha + 2.7\alpha^2)]/(1 + 2\alpha)$  for S/W = 4 and  $f(\alpha) = 1.9109 - 5.1552\alpha + 12.6880\alpha^2 - 19.5736\alpha^3 + 15.9377\alpha^4 - 5.1454\alpha^5$  for S/W = 5. The average  $K_{\rm Ic}$  value is calculated from at least three valid tests. The fracture surface energy  $(\gamma)$  is then calculated from the assumption that  $\gamma$  is equal to  $G_{\rm C}/2 = K_{\rm Ic}^2(1 - \nu^2)/2E$ . **2.4. Experimental UV—vis Spectroscopy.** The optical trans-

**2.4. Experimental UV–vis Spectroscopy.** The optical transparency of LiAlB2 (2 GPa compressed lithium aluminoborate glass) was investigated on a specimen with a thickness of 1.36 mm, polished to an optical finish using 3  $\mu$ m diamond paste. An ultraviolet–visible (UV–vis) spectrometer (Cary 50 Bio, Varian) was used to measure the baseline-corrected transmittance of the sample in the wavelength

range of 200-1000 nm. Based on the absorbance data, we calculated the transmittance in percentage as shown in Figure S2 in the Supporting Information. Three different areas (at least 1 mm away from each other) were tested to ensure the reliability of the obtained

2.5. Experimental Powder X-ray Diffraction Analysis. Asmade and compressed glass samples were crushed in a mortar before being loaded onto a zero-background plate (monocrystalline silicon). X-ray diffraction measurements were acquired using a Panalytical Empyrean diffractometer in a  $\theta$ - $\theta$  geometry using a  $\tilde{\text{Cu}}$  K $\alpha_1$  source ( $\lambda$ = 1.54098 Å) in the range of  $2\theta = 5 - 70^{\circ}$ .

2.6. MD Simulations of Glass Formation. Glasses of composition 25Li<sub>2</sub>O-20Al<sub>2</sub>O<sub>3</sub>-55B<sub>2</sub>O<sub>3</sub>, 35Na<sub>2</sub>O-20B<sub>2</sub>O<sub>3</sub>-45SiO<sub>2</sub>, and 13Na<sub>2</sub>O-6MgO-10CaO-71SiO<sub>2</sub> were simulated using a GPU-accelerated<sup>31</sup> version of LAMMPS.<sup>32</sup> Using a recently parameterized force field, <sup>33,34</sup> we prepared the glasses with varying pressure treatments (0, 0.5, 1.0, and 2.0 GPa), ultimately mimicking the experimental procedure described above. For the LiAlB glass, we tried to increase the simulation pressure further but found crystallization to start appearing at a pressure of around 4 GPa. We thus limit the maximum pressure to 2.0 GPa, for which no crystals were observed in any of the samples.

First, 10,000 atoms were randomly placed in a cubic simulation box while avoiding any unrealistic proximity of atoms. This was followed by potential energy minimization and initial mixing of the structures at 2500 K for the LiAlB and NaBSi glasses and at 3500 K for the SLS glass in the NPT ensemble for 100 ps at 0.1 GPa for the 0 GPa sample, while the other samples were subjected to pressures of 0.5, 1.0, and 2.0 GPa, respectively. This step was used to obtain equilibrium liquids of meaningful densities and was followed by additional mixing for 100 ps at 3000 K for the LiAlB and NaBSi glasses and at 3500 K for the SLS glass in the NVT ensemble and another 700 ps of mixing in the NPT ensemble at 2500 K for the LiAlB and NaBSi glasses and at 3500 K for the SLS glass at the previously designated pressures. This step was proceeded by quenching the structures to 300 K at 1 K ps<sup>-1</sup> in the *NPT* ensemble. Here, during cooling, the pressure was linearly released from 0.1 to 0.0 GPa for the 0 GPa sample, while the remaining samples were maintained at their designated pressures. Next, when reaching 300 K, all structures were subjected to 100 ps of relaxation in the NPT ensemble at 300 K and the designated pressure. Final relaxations were performed for another 100 ps in the NPT ensemble at 300 K and zero pressure. This was found to be adequate for ensuring convergence of energy and volume. We found that the volume had typically relaxed after a few picoseconds of relaxation time (see example of the relaxation for the LiAlB glass quenched at 2 GPa in Figure S3 in the Supporting Information). Note that, despite such zero-pressure relaxation, the formed glasses remain permanently densified. All procedures in the quenching process and following analyses employed a time step of 1 fs, a Nosé-Hoover thermostat, and, when applicable, a Nosé-Hoover barostat. We performed each pressure-quenching six times to ensure proper statistics of the obtained results, and all shown simulation results are therefore averages of the six independent structures of each pressure.

2.7. MD Simulations of Elastic Properties. Elastic constants were obtained by subjecting the quenched species to stepwise elongations of  $\varepsilon = 0.0001 = 0.01\%$  in the tensile directions xx, yy, and zz as well as in the shear directions xy, xz, and zy under the assumption of isotropic structures. After each elongation step, the structures were relaxed for 1 ps at 300 K before simulating for another 1 ps, while averaging the measured stress in the given direction (sampling at every time step), both procedures in the NVT ensemble. 70 elongations were performed in each direction. After recording the stress-strain curves, linear regression was performed to obtain the elastic constants of the systems. Moreover,  $C_{11}$  and  $C_{44}$  were evaluated as averages of  $C_{11}$ ,  $C_{22}$ , and  $C_{33}$  as well as of  $C_{44}$ ,  $C_{55}$ , and  $C_{66}$ , respectively. Based on the assumption of isotropy,  $C_{12}$  was then calculated as 35

$$C_{12} = C_{11} - 2C_{44} \tag{6}$$

This enabled calculation of the Young's modulus (E) and Poisson's ratio  $(\nu)$  as follows<sup>33</sup>

$$E = \frac{(C_{11} - C_{12})(C_{11} + 2C_{12})}{C_{11} + C_{12}}$$
(7)

$$\nu = \frac{C_{12}}{C_{11} + C_{12}} \tag{8}$$

2.8. MD Simulations of Fracture Toughness. Fracture toughness  $(K_{Ic})$  of the simulated glasses was calculated using the approach of Brochard,  $^{36}$  which has the advantage that it is able to estimate  $K_{\rm Ic}$  of both brittle and plastic fractures.  $^{26,36,37}$  We here briefly summarize the approach. First, structures of 10,000 atoms were replicated into  $1 \times 2 \times 2$  supercells. Then, cationic atoms were removed in an ellipse with a width of 1/3 of the longest side of the simulation box and a height of 1/5 of the width. In the used force field parameterization, the oxygen charge is determined by the glass composition, and thus, oxygens were then removed iteratively from the ellipse to match the original composition before the oxygen charge was redefined for the new composition to ensure charge neutrality. The change of oxygen charge was maximally around 0.00002 units of formal charge. Before proceeding with fracture, precracked samples were subjected to energy minimization followed by 1 ns of relaxation at 0 GPa pressure in the NPT ensemble at 300 K followed by another energy minimization where the box boundaries were allowed to relax to 0 GPa pressure.

Then, fracture experiments were conducted by first equilibrating the structures for 100 ps in the NVT ensemble before stepwise deforming the simulation box in the plane normal to the precrack (zdirection) using strain steps of  $\varepsilon = 0.01 = 1\%$ . All fracture steps were performed at 300 K. In-between each step, the structure was first minimized and then equilibrated for 5 ps before averaging the stress in the strain direction for another 5 ps by sampling the stress at every time step. This sequence was repeated until reaching a strain of 110%. All probed structures saw full fracture before reaching the maximum strain. A stress-strain curve was obtained, and the critical energy release rate  $(G_c)$  was found by integration as follows

$$G_{\rm c} = \frac{L_{\rm x}L_{\rm y}}{\Delta A_{\infty}} \int_{L_{z,0}}^{L_{z,\rm max}} \sigma_z \mathrm{d}L_z \tag{9}$$

where L designates the simulation box length,  $\Delta A_{\infty}$  is the crack surface area obtained upon full fracture, and  $\sigma_z$  is the recorded stress in the z-direction. The fracture toughness was then calculated by

$$K_{\rm Ic} = \sqrt{\frac{G_{\rm c}E}{1 - \nu^2}} \tag{10}$$

where E and  $\nu$  were taken from the previous simulations of elastic properties.

Finally, we have tested the effect of the crack-to-box size ratio on  $K_{\rm Ic}$ , showing no significant variation as presented in Figure S4 in the Supporting Information. Furthermore, we note that the employed strain-rate is significantly lower than what was previously found to cause strain-rate dependencies of  $K_{\rm Ic}$ . Although not all studies use the NVT ensemble for studying fracture mechanics, 40,41 the use of it has in a number of cases provided a good description of fracture toughness for both classical and reactive potentials.

2.9. MD Simulations of the Coordination Number and Bond Switching Analysis. During the fracture simulations, the atomic arrangement is changed as a result of the deformation. The breaking and formation of bonds are studied by analyzing the change in the coordination number (CN) and the bond switching events during fracture.<sup>22</sup> The CN of a central atom (i.e., Li, Na, Mg, Ca, Si, B, and Al) is defined as the number of oxygen atoms within a given cutoff distance from this central atom. The cutoffs were obtained from the partial pair correlation functions of a glass quenched at 0 GPa as the distance where the function reached zero after the first peak or where the minimum after the first peak was observed. The found cutoff

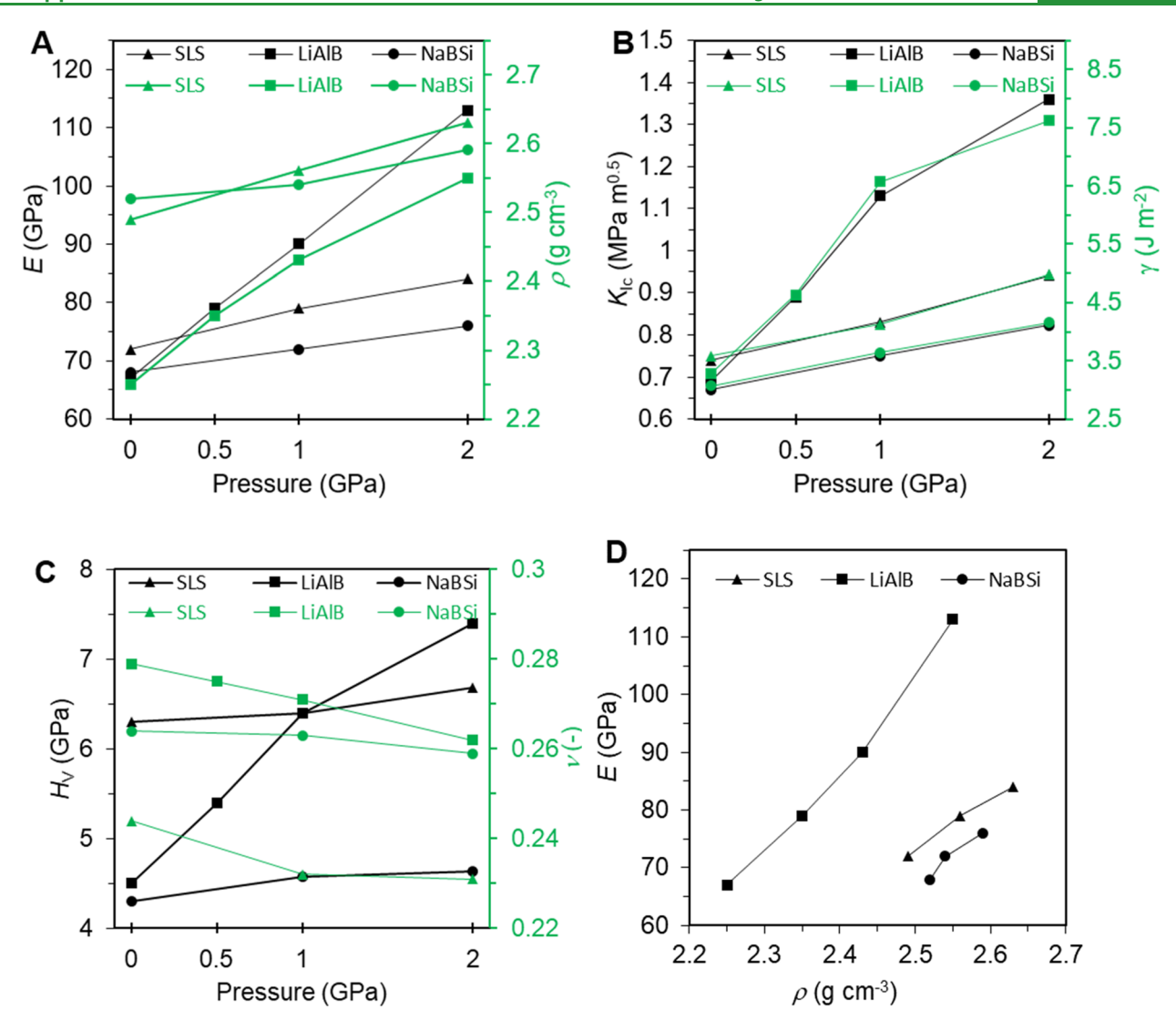


Figure 2. Pressure dependence of experimentally measured properties. (A) Pressure dependence of Young's modulus (E) and density ( $\rho$ ). (B) Pressure dependence of fracture toughness ( $K_{\rm Ic}$ ) and energy (γ). (C) Pressure dependence of Vickers hardness ( $H_{\rm V}$ ) and Poisson's ratio ( $\nu$ ). (D) Dependence of E on  $\rho$ . Estimated errors for E,  $\rho$ ,  $K_{\rm Ic}$ ,  $\gamma$ ,  $H_{\rm V}$ , and  $\nu$  do not exceed 1 GPa, 0.005 g cm<sup>-3</sup>, 0.03 MPa m<sup>0.5</sup>, 0.05 J m<sup>-2</sup>, 0.05 GPa, and 0.005, respectively.

distances were 1.8 Å for B-O, 2.1 Å for Al-O, 1.9 Å for Si-O, 2.4 Å for Li-O, 2.9 Å for Na-O, 2.4 Å for Mg-O, and 2.9 Å for Ca-O. The fraction of atoms with an increased, decreased, or unchanged CN is obtained by comparing the CN of each individual atom with its initial CN (at zero strain). The swapped CN indicates that the CN is unchanged, but the atom is bonded to at least one different oxygen atom (distinguished using the individual ID of each atom) compared to its initial configuration (at zero strain). In addition to calculating the fraction of atoms that are involved in bond switching throughout the entire volume of the glass, we visualized the spatial distribution of such events by performing the same calculation for smaller volumes. 100 × 100 points in the plane perpendicular to the direction of the precrack were selected to represent the pixels in the visualization, and the fraction of atoms with changes in the CN (increased, decreased, swapped, or the sum of all three) was calculated for all atoms within a circle of radius 4 Å around each point, thus using cylindrical volumes.

**2.10.** MD Simulations of Permanent Angle Deformation Analysis. During the fracture simulations, the bonds in the glass network stretch and rotate, resulting in atomic rearrangement. These changes are analyzed by considering the bond angles in the precracked box of the simulated glass. We study the bond angle changes in the LiAlB glass as this composition features the most pronounced increase in  $K_{\rm Ic}$  with pressure. We follow a procedure for

such angular deformation analysis of a non-precracked box from a previous study.  $^{43}$  The changes of the B–O–B, Al–O–B, and Al–O–Al angles are recorded from oxygens with a CN of 2 (using the same cutoffs as presented earlier) while applying the tensile stress from 0% to 110% strain. The permanent average angle deformation is calculated as the difference between the bond angles at 110% strain relative to the initial bond angles at zero strain.

**2.11.** MD Simulations of Brittleness Index. The brittleness index (B) was calculated based on the methodology of Wang et al. The method relies on analyzing the stress—strain curve of the fracture process to separate it into an elastic and plastic part. From the elastic part, an elastic contribution to the total energy release rate may be obtained  $(G_{\rm el})$ . Here, we identify the transition from the elastic to plastic part as the strain of the first stress maximum. In a fully brittle material, the stress will drop sharply from a maximum value down to zero stress at fracture, while in a plastic material, structural rearrangement will be induced during the fracture process, resulting in a plateau and/or a nonsharp decrease of stress in the stress—strain curve. The degree of brittleness is then determined from the brittleness index (B)

$$B = \frac{G_{\rm el}}{G_{\rm c}} \tag{11}$$

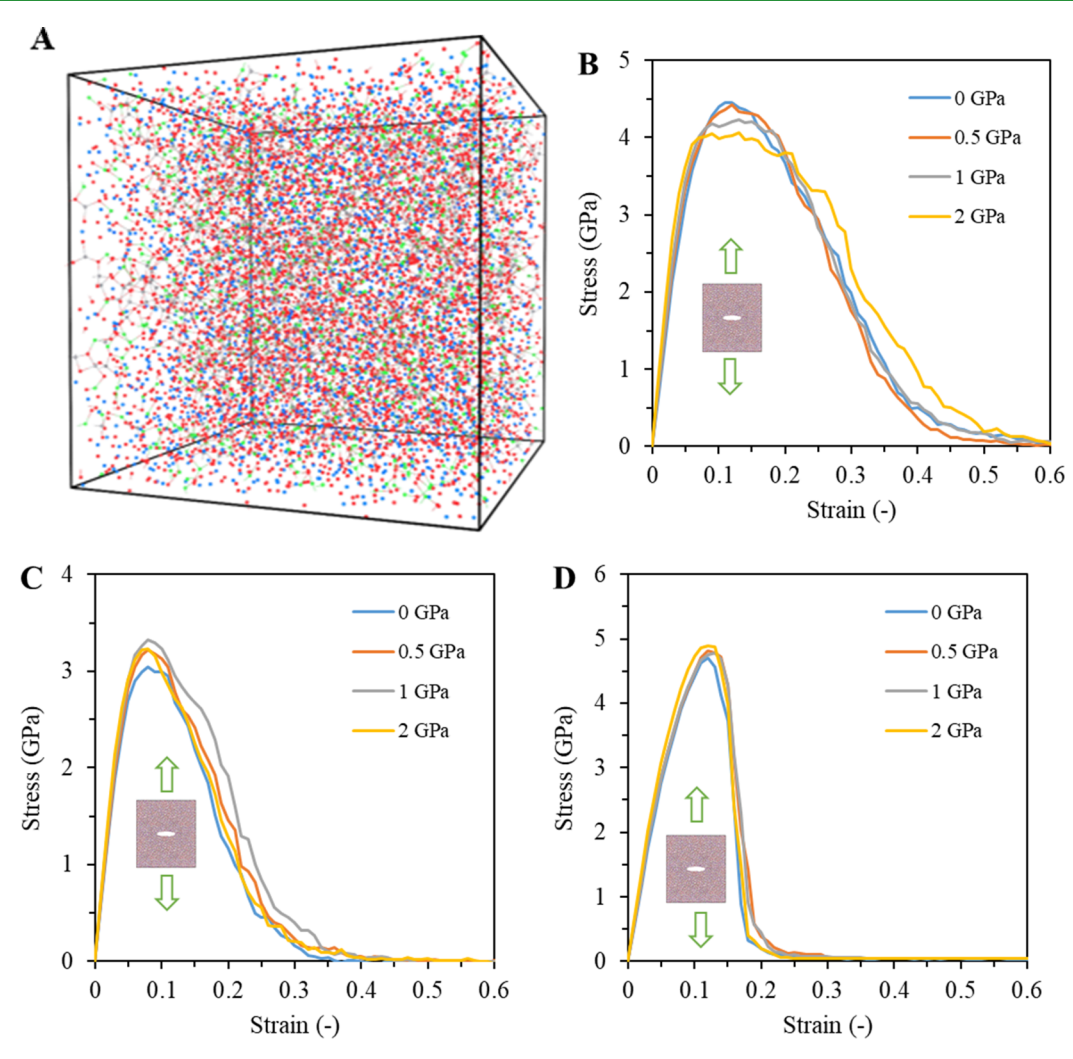


Figure 3. Simulations of fracture toughness. (A) Example of a simulated as-made (0 GPa)  $25\text{Li}_2\text{O}-20\text{Al}_2\text{O}_3-55\text{B}_2\text{O}_3$  glass. Green is lithium, blue is boron, gray is aluminum, and red is oxygen. (B) Stress—strain curves for all probed LiAlB glasses, showing slightly decreasing maximum stress and increasing tailing upon increasing degree of densification. (C) Stress—strain curves for all probed NaBSi glasses, showing slightly increasing both maximum stress and tailing from 0 to 1 GPa and decreasing from 1 to 2 GPa. (D) Stress—strain curves for all probed SLS glasses. No major differences of the curves are found in the case of the SLS glasses.

where B = 1 indicates a perfectly brittle fracture, while B decreases as the ductility of the system increases. The obtained values of B were averaged over the six obtained structures for each pressure treatment.

# 3. RESULTS AND DISCUSSION

3.1. Mechanical Properties. Figure 1 presents the singleedge precracked beam setup to measure the fracture toughness of the studied glasses. The self-consistent SEPB method consists of three steps, i.e., indentation, precracking, and fracturing (see the Methods section). The precrack represents the flaw in glasses, typically introduced during production, transport, or final usage. Figure 1A shows an indentation line made with a load of 10 N and spaced with 100  $\mu$ m between adjacent indents on the 2 GPa compressed lithium aluminoborate glass. The corner cracks are connected, occurring when two indents are placed close to each other (effect of indentation residual stress), leading to the fabrication of a precrack of meaningful quality (i.e., even and straight). Figure 1B shows typical load—displacement curves of the three indented glasses densified at 2 GPa and an image of the used bridge-compression fixture (inset). To produce a precrack with a length of around 50% of the specimen width (W), the

compressive load needs to be around 80 N for sodium borosilicate and 100 N for soda-lime-silica and lithium aluminoborate glasses. This difference is likely due to the lower resistance to indentation crack initiation of the sodium borosilicate glass relative to the other two glasses.<sup>24</sup> The slopes of the load-displacement curves in Figure 1B reveal that the lithium aluminoborate glass is the most rigid and the sodium borosilicate glass is the least rigid, in good agreement with the variation in Young's modulus as measured by ultrasonic echography (see Table S2 in the Supporting Information). Figure 1C shows the typical load-displacement curves of the three precracked glasses densified at 2 GPa and an image of the three-point bending fixture (inset). All curves show unstable fracture at the maximum load, which is required for removing the influence of stress-corrosion.<sup>25</sup> Lithium aluminoborate glass has the highest maximum load, and as a result, it possesses the highest fracture toughness  $(K_{Ic})$  of the three compositions. A post-fractured specimen is shown in Figure 1D, with the visible indentation line. The uneven state of the precrack front is acceptable (<10%) as noted in the ASTM standard, 16 and the precrack length is taken as the average from measurements at 25, 50, and 75% of the broadness (B).

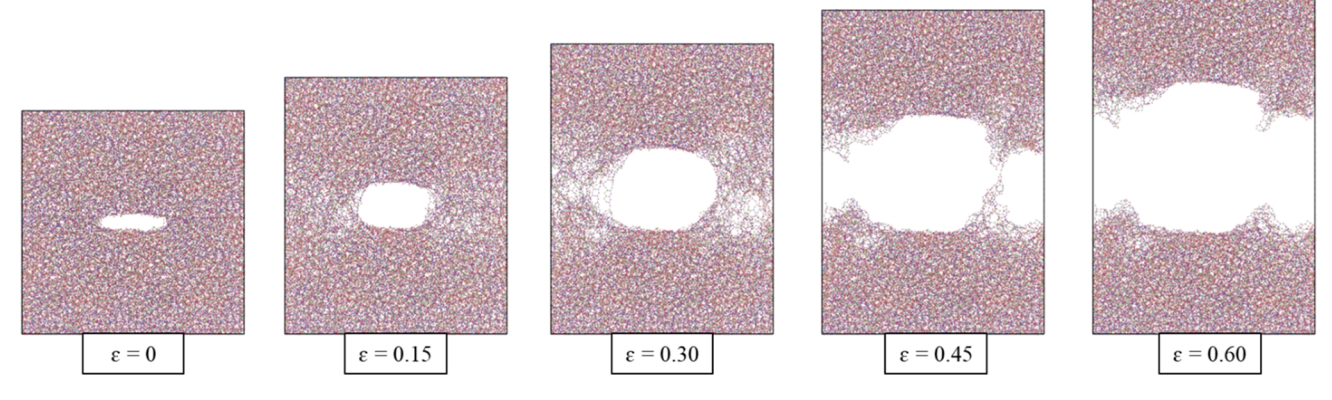


Figure 4. Evolution of fracture in the simulated as-made lithium aluminoborate glass under forced elongation at strains of 0, 0.15, 0.30, 0.45, and

The values of  $K_{Ic}$  of all samples are presented together with Young's modulus (E), Poisson's ratio ( $\nu$ ), density ( $\rho$ ), Vicker's hardness  $(H_V)$ , and fracture surface energy  $(\gamma)$  in Figure 2 and Table S2 in the Supporting Information. Upon high-temperature pressure treatment (so-called hot compression), the studied glasses become denser, harder, stiffer, and tougher. However, densified glasses generally show a decrease in their resistance to crack initiation under a sharp indentation tip. 9,44 We note that the glasses remain densified after decompression and cooling and all properties are stated for the permanently densified glasses in ambient conditions. Figure 2A shows the pressure dependence of E and  $\rho$ . We observe a pressure-induced increase in E as found in previous studies <sup>9,45,46</sup> as well as a decrease in  $\nu$  for all glasses (Figure 2A,C). Upon hot compression at 2 GPa, E increases from 72 to 84 GPa, 67 to 113 GPa, and 68 to 76 GPa for soda-lime-silica, lithium aluminoborate, and sodium borosilicate glasses, respectively. This dramatic change, primarily for the lithium aluminoborate, can be explained by the simultaneous transformation of both B<sup>III</sup> to B<sup>IV</sup> and Al<sup>IV</sup> to Al<sup>V</sup> and Al<sup>VI9</sup> as well as the increase in density (Figure 2D). Indeed, the lithium aluminoborate glass exhibits the largest increase of E,  $\rho$ , and  $H_V$  upon compression among the three glasses (Figure 2A,C). Figure 2B shows that  $K_{\rm Ic}$  and  $\gamma$  increase with increasing pressure for all glasses, yet the increase for the lithium aluminoborate glass is remarkably higher than those for the silicate and borosilicate glasses. The as-made value of  $K_{Ic}$  for all three glasses is around 0.7 MPa  $m^{0.5}$ , but then  $K_{Ic}$  increases to 0.94, 1.36, and 0.82 MPa  $m^{0.5}$  for the silicate, aluminoborate, and borosilicate glasses, respectively, upon hot compression at 2 GPa. Notably, to our knowledge,  $K_{Ic}$  of 1.36 MPa m<sup>0.5</sup> is a record-high value for bulk oxide glasses and also higher than those of silicon oxynitride and oxycarbide glasses as measured using a self-consistent method.<sup>23,4</sup>

3.2. Molecular Dynamics Simulations. We next study the atomistic origins of the above measured changes in properties upon compression in order to reveal the design concepts for stronger (harder) and tougher (damage-tolerant) bulk oxide glasses. To this end, we have performed classical molecular dynamics (MD) simulations of the lithium aluminoborate glass featuring record-high fracture toughness as well as the other two glasses studied experimentally. For the lithium aluminoborate glass, we initially validate the simulations, using a recently developed interatomic potential,<sup>33</sup> by comparing computed values of  $\rho$  and average B and Al

coordination of six lithium aluminoborate glasses (25Li<sub>2</sub>O $xAl_2O_3$ -(75 –  $x)B_2O_3$  with x varying from 0 to 25 mol %) with experimental values<sup>48</sup> (Figure S5 in the Supporting Information). We generally find good agreement between experiments and simulations. Then, we simulated 25Li<sub>2</sub>O<sub>3</sub>-20Al<sub>2</sub>O<sub>3</sub>-55B<sub>2</sub>O<sub>3</sub> glasses, which have been quenched from the liquid to glassy state under pressure (0, 0.5, 1.0, and 2.0 GPa) as described in detail in the Methods section. The simulated  $\rho$  and average B and Al coordination numbers are found to agree well with experiments<sup>9</sup> (Figure S6 in the Supporting Information) despite some differences in the absolute values of the Al coordination number. Since all the trends are qualitatively captured by the simulations, we can use them to understand the pressure-induced changes in deformation and fracture mechanisms on the atomic scale. However, the lack of absolute agreement of Al coordination between experiments and simulations may affect the quantitative estimations of toughness. However, we note that all Al coordination states (IV, V, and VI) are present in the MD simulations, offering some representation of their behavior in the performed fracture simulations. Moreover, elastic moduli show good agreement between simulations and experiments for all glasses (see Table S2 in the Supporting Information), although we note that the SLS glasses feature slightly underestimated elastic moduli compared to the experimental results.

Figure 3A shows a snapshot of the atomic structure of the as-prepared lithium aluminoborate glass. After manually inserting a precrack in the network, the structure is relaxed toward a stable energy configuration of zero pressure. Next, we start stepwise deformations of the simulation box (strain steps of  $\varepsilon = 1\%$ ) along the direction normal to the plane of the introduced precrack (mode I) to force stress generation at the crack tips and ultimately opening of the crack. The stress along the deformation direction is recorded at every time step and afterward averaged over the last 5 ps of simulation at each strain step during the stepwise deformations. The obtained stress-strain curves for all lithium aluminoborate glasses are shown in Figure 3B (0-2 GPa pressure treatments), all having the same crack-to-box-size-ratio. We present similar curves for the NaBSi and SLS glasses in Figure 3C,D, respectively. In the stress-strain curves, the LiAlB glass has the longest tail while the SLS glass has the shortest tail after reaching the maximum stress among the three glasses. While we note that the used interatomic potential has not strictly been parameterized for describing fracture, the fracture toughness of a number of

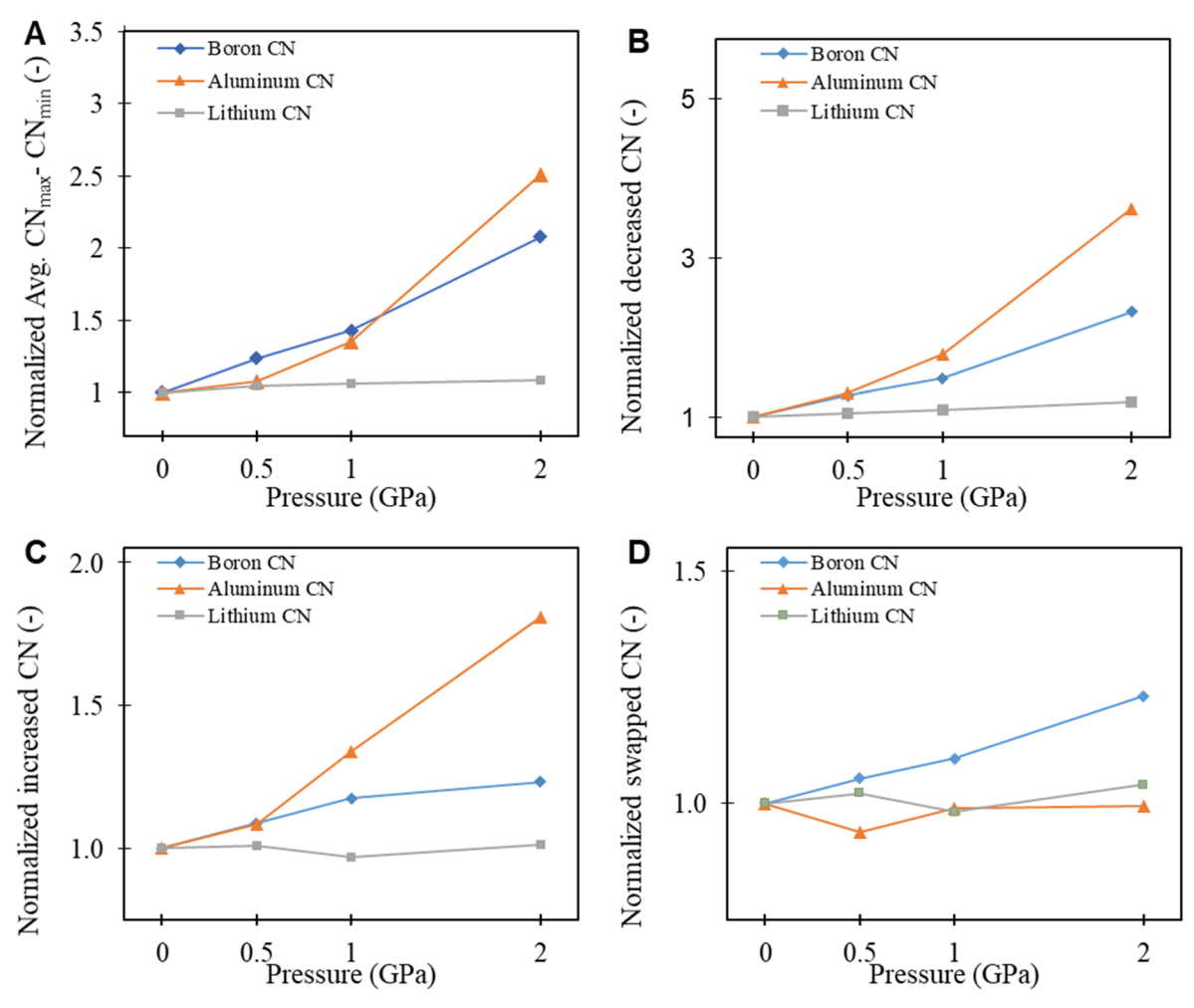


Figure 5. Atomic transformations in lithium aluminoborate glass during fracture by molecular dynamics simulations. (A) Pressure dependence of average CN differences between minimum ( $\varepsilon \approx 0.2$ ) and maximum ( $\varepsilon = 0$ ) CNs during the tensile stress experiment, i.e.,  $\text{CN}_{\text{max}} - \text{CN}_{\text{min}}$  of the data taken from Figure S10 in the Supporting Information, normalized by the value of the as-made (0 GPa) glass. (B) Pressure dependence of the fraction of atoms of the decreased CN after complete fracture normalized by the value of the as-made glass. The decreased CN occurs when the bonds are broken during tensile stress. (C) Pressure dependence of the increased CN normalized by the increased CN fraction of the as-made glass. The increased CN occurs when the central atom (boron, aluminum, or lithium) connects to more oxygen atoms after fracture compared to before fracture (see Figure 6A for an example). (D) Pressure dependence of the swapped CN normalized by the swapped CN fraction of the as-made glass. The swapped CN occurs when the core atom is bonded to the same number of oxygen atoms, but one or more oxygen atoms have been substituted with another oxygen atom during the fracture simulation (see Figure 6B for an example).

glasses has been found to be well-described using nonreactive potentials.<sup>37</sup> In addition, as described below, we find good agreement between  $K_{\rm Ic}$  obtained from simulations and experiments.

Figure 4 presents an example of the evolution of the structure for the as-made LiAlB glass upon deformation of the precracked glass from 0 to 60% strain. We note that regions around the crack tip show continuous bond stretching (Figure 4, 15 and 30% strain) before experiencing crack growth and ultimately full fracture (Figure 4, 45 and 60% strain). This phenomenon is also found in the compressed LiAlB glasses, explaining the stable fracture in all curves of Figure 3B. On the other hand, we find that the maximum stress decreases while the length of the "tail" increases with increasing pressure. This is due to an increase in the degree of ductility in the densified glasses. To rule out that the tailing of the stress-strain curves in Figure 3 (especially in the case of the LiAlB glasses) is a spurious effect of the used potential type, we have simulated the stress-strain curve upon mode I fracture of glassy SiO<sub>2</sub>. As shown in Figure S7 in the Supporting Information, we find it

to be highly brittle, as also reported in another work using different interatomic potentials.<sup>37</sup> This thus confirms the reliability of the used potential to study glass fracture and confirms that the ductile behavior of the LiAlB glass is a consequence of its composition/structure rather than a defect of the present forcefield.

The permanent densification results in a steeper initial increase in the stress (Figure 3), in agreement with the experimentally and computationally observed pressure-induced increase in Young's modulus. Based on these data, we compute the critical energy release rate ( $G_{\rm C}$ ) and  $K_{\rm Ic}$ .  $G_{\rm C}$  and  $K_{\rm Ic}$  are found to be 11.32 J m $^{-2}$  and 0.94 MPa m $^{0.5}$ , 11.64 J m $^{-2}$  and 1.05 MPa m $^{0.5}$ , and 11.54 J m $^{-2}$  and 1.11 MPa m $^{0.5}$  for asprepared, 1 GPa hot-compressed, and 2 GPa hot-compressed LiAlB glasses, respectively (Table S2 in the Supporting Information). As in the experiment, the simulated LiAlB glasses have the highest pressure dependence of  $K_{\rm Ic}$ , thus featuring a more pressure-sensitive response than the two other glasses (Figure S8 in the Supporting Information). We note that it has been claimed that bulk oxide glasses can only be

toughened by introducing fibers or particles of other glasses or ceramics in the glass matrix, i.e., only by extrinsic toughening.<sup>3,49</sup> However, our results show that hot compressing the glass leads to increasing coordination numbers (CNs) in the glass structure, resulting in increasing ductility (Figure 3B) and hence increasing toughness. This means that intrinsic toughening is possible (see the following paragraphs). These simulated K<sub>IC</sub> values show reasonable absolute agreement with the experimental ones and feature the same qualitative pressure dependence. For LiAlB glasses, the slight difference between simulated  $K_{Ic}$  and experimental  $K_{Ic}$  values may be due to the lower average coordination number of Al in the simulations (Figure S6 in the Supporting Information). Overall, the  $K_{Ic}$  of the LiAlB glasses from both MD simulations and SEPB experiments is found to increase with increasing compression (Table S2 in the Supporting Information), in agreement with the observed increase in nanoductility as illustrated in Figure 3B. For the NaBSi and SLS glasses,  $K_{Ic}$  generally increases with pressure yet at a noticeably smaller extent than for the LiAlB glasses. In addition, the simulated NaBSi 2 GPa glass is found to have a lower  $K_{Ic}$  than the NaBSi 1 GPa glass, indicating the possibility of a saturation of the toughening mechanism, although this is not observed in the experimental data. Moreover, we have quantified the degree of nanoductility for the as-prepared and hot-compressed LiAlB glasses by calculating the brittleness index (B), where B = 1 indicates a perfectly brittle fracture while B will decrease for increasing degree of ductility (see Methods for details). We find that B decreases from 0.30 to 0.17 upon hot-compression of the asprepared glass at 2 GPa (Figure S9 in the Supporting Information).

The MD simulations can then be used to reveal the structural origin of the pressure-induced increase in ductility. For example, the CNs of boron and aluminum in LiAlB glasses increase more upon compression than that of lithium. For boron, the fraction of B<sup>III</sup> decreases while that of B<sup>IV</sup> increases. For aluminum, the fraction of Al<sup>IV</sup> decreases while those of Al<sup>V</sup> and AlVI increase (Figure S11 in the Supporting Information). When the glasses with a precrack are subjected to tensile stress, we observe that, for both as-prepared and compressed glasses, Li exhibits more pronounced changes in the CN relative to B and Al (Figure S10 in the Supporting Information). This is likely due to the ionic character of the Li-O bonds, which tend to easily break under load as compared to the stronger ionocovalent B-O and Al-O bonds. 43 By comparing the minimum CN value (at  $\varepsilon \approx 0.2$ ) to the initial CN value, we find that the CN changes of both B and Al under the tensile stress depend on the pre-densification, but this is not the case for Li (Figure 5A). This suggests that B and Al are the main contributors to the rise of plasticity in the compressed LiAlB glasses as described in the next section.

**3.3. Plasticity Mechanism of High-Toughness Densified Glass.** To understand the plasticity mechanism, we analyze the extent of bond switching <sup>22</sup> in the simulated glasses, i.e., the extent to which atomic coordination numbers increase, decrease, and swap as a function of strain during the tension of the precracked glass. By performing such analysis, we find that for the lithium aluminoborate glasses, the increasing extent of plasticity upon densification arises from the higher extent of the decreased CNs of Al and B, the increased CN of Al, and the swapped CN of B (Figure 5B–D). Using the fraction of atoms with the changed (increased, decreased, or swapped) CN after fracture compared to the structure at zero strain, we

normalized all changed CN fractions by the value of the asmade (0 GPa) glass. We note how this primarily allows for internal comparison between glasses of similar composition. The decreased CN shows the number of bonds that breaks by tensile stress. The increased CN is a mechanism where the central atom (e.g., Al) is bonded to more oxygen atoms after fracture compared to its initial state, while the swapped CN refers to the situation when the core atom (e.g., B) retains its local environment but changes neighboring oxygen atoms similar to the mechanism previously described for SiO<sub>2</sub>. <sup>20,21</sup> Comparing with the as-made glass, the increased CN of Al and the swapped CN of B in the 2 GPa compressed glass rise ~1.8 and ~1.25 times, respectively. The accumulated rise in events that increase, decrease, or swap the coordination number in the compressed glasses leads to more atomistic translation and rotation, allowing more deformation under stress before experiencing fracture. As such, the coordination defects introduced in the glass network by hot-compression act as local reservoirs of plasticity, which effectively dissipate elastic energy via irreversible structural reorganizations (e.g., bond switching) rather than by breaking. Our analysis thus suggests that this is the main mechanism responsible for the increased plasticity in the densified LiAlB glasses (Figure 3B). We performed a similar analysis for the SLS and NaBSi glasses. As shown in Figure S12 in the Supporting Information, similar tendencies for the decreasing CN are observed for most of the studied glasses while some differences exist for the increasing and swapped CNs. Notably, for the NaBSi glasses, the swapping and increasing CNs seem to increase up to compression at 1 GPa and then drop when increasing the pressure to 2 GPa, corresponding to the trend of first increasing and then decreasing  $K_{Ic}$  with pressure for the same simulated glasses. For the SLS glasses, a deviation from linearity of  $K_{Ic}$  vs pressure for the 1 GPa compressed glass (lower  $K_{Ic}$  than expected from interpolation) is seen. A similar deviation in linearity is seen for the decreasing CN of Si (Figure S12 in the Supporting Information), thus suggesting a connection to the fracture mechanism and ultimately the estimated  $K_{Ic}$ . In general, for the LiAlB glasses, Li tends to swap the CN more easily than Al, which in turn swaps the CN more easily than B (25, 12, and 7.5% for Li, Al, and B, respectively, see Figure S13 in the Supporting Information). This may be due to the ionic character of the Li-O bond. Generally, for all systems, we find that the changes in CN and changes of neighbors are somewhat more enhanced for network formers (Al, B, Si) than for modifier ions (Figure 5 and Figure S12 in the Supporting Information). However, when comparing the different glasses, the absolute number of bond switching events varies significantly, with mainly B and Al atoms undergoing large absolute increases, especially in the LiAlB glasses (Figure S13 in the Supporting Information). These results suggest that the amounts of bond switching events are more pronounced in the densified LiAlB glasses relative to that in the densified NaBSi and especially SLS glasses, in agreement with the higher  $K_{\rm Ic}$  in the densified LiAlB glasses. This is likely due to the presence of both B and Al atoms, which both favor bond switching and the mobile Li ions that change their structural role depending on the Al and B coordination states. While amorphous oxides such as Al<sub>2</sub>O<sub>3</sub> and  $SiO_2$  have been shown to swap and change the CN during tension/compression on the nanoscale, <sup>20–22</sup> here, we have found the rise of the bond switching events to be enhanced

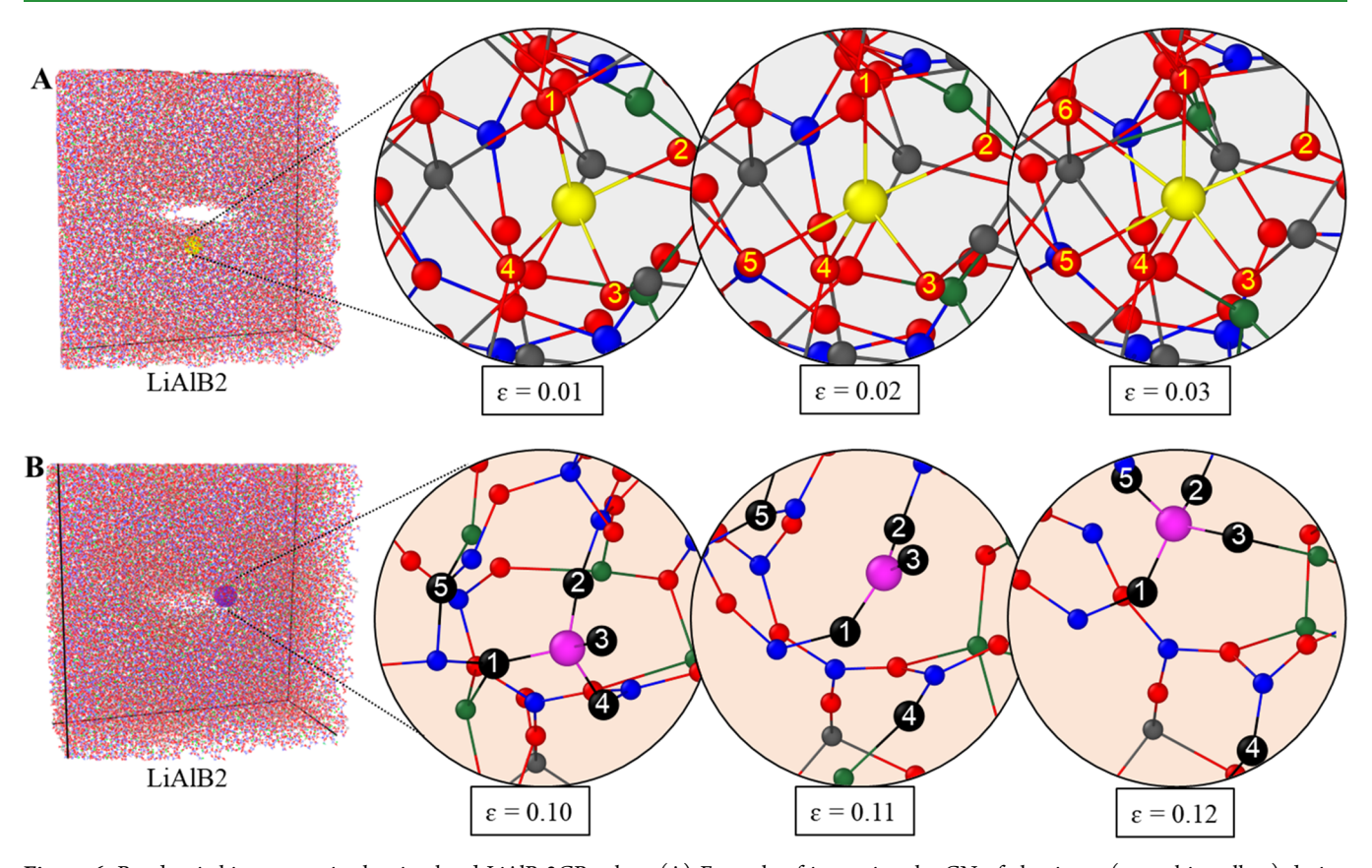


**Figure 6.** Bond switching events in the simulated LiAlB 2GPa glass. (A) Example of increasing the CN of aluminum (central in yellow) during fracture. The CNs of aluminum are 4 at  $\varepsilon$  = 0.01, 5 at  $\varepsilon$  = 0.02, and 6 at  $\varepsilon$  = 0.03. In both panels (A) and (B), green is lithium, blue is boron, gray is aluminum, and red is oxygen. (B) Example of a swapped CN of boron (central in purple) first connected to four oxygens (numbers 1, 2, 3, and 4), then to three oxygens (oxygen number 4 is disconnected), and finally to four oxygens again (with the new oxygen number 5) at  $\varepsilon$  = 0.10, 0.11, and 0.12, respectively.

when the oxide glass is densified, ultimately providing a route to control the plasticity of the glassy system.

Figure 6A,B shows individual atomic snapshots of the increased CN and swapped CN events, respectively, during fracture simulations of the LiAlB glasses precompressed at 2 GPa. In Figure 6A, the Al atom (central yellow) having a CN of 4 at  $\varepsilon=0.01$  increases its CN to 5 at  $\varepsilon=0.02$  and to 6 at  $\varepsilon=0.03$ , indicating an increased CN of 2 for Al. In Figure 6B, the B atom (central purple) having CN of 4 at  $\varepsilon=0.10$  decreases its CN to 3 at  $\varepsilon=0.11$  and then increases its CN back to 4 at  $\varepsilon=0.12$  with a new oxygen (O) atom, indicating one swapped CN for B. Both atomic mechanisms occur at low strain values ( $\varepsilon<0.2$ ,Figure 3B), highlighting the important role of structural transformations prior to fracture on the total plastic deformation and resulting  $\gamma$  and  $K_{\rm Ic}$  values.

In addition to the presented generalized bond switching analysis, we performed spatial visualization of different events (decreased, increased, and swapped CNs for B and Al) in the as-made (0 GPa) and 2 GPa compressed LiAlB glasses (see Figure S14 in the Supporting Information), generally showing how bond switching events for B and Al mainly occur near the crack tips and crack propagation path. The structural rearrangements are not solely observed at the fracture surface as it would be expected for a perfectly brittle material, but they also occur in the bulk glass. This allows for local deformation and dissipation of stress, thus enhancing the nanoductility. Notably, the events where the B and Al atoms decrease their CNs are observed to be more widely distributed across the

volume, whereas the bond swapping events are mostly concentrated near the crack propagation path. Compared to the as-made glass, bond switching events are more pronounced in the compressed glass and the zones of high structural rearrangement are observed to extent further away from the crack propagation path. Again, this reveals how the structure of the compressed LiAlB glass allows for a larger amount of structural rearrangement, ultimately increasing its nanoductility and toughness.

Moreover, we have also analyzed the deformations of interatomic angles<sup>43</sup> during the fracture process for the LiAlB glasses. Here, we calculate the B-O-B, Al-O-B, and Al-O-Al angles (for two-coordinated oxygens) as a function of strain in the simulation setup (Figure S15A-C in the Supporting Information). For all the investigated angles, the higher the pressure, the smaller the obtained angles, in agreement with the increase of the CN upon hot compression (Figures S10 and S11 in the Supporting Information). Under tensile stress, the angles increase with increasing strain until a macroscopic strain of the box of  $\sim$ 0.2 (i.e., immediately following the strain of the maximum stress), where the network bonds begin breaking. At higher strains, the angles start decreasing toward a new constant value. Overall, we find a permanent deformation of the interatomic angles, which we quantify by calculating the difference between the initial and post-fracture average angles. For the B-O-B, B-O-Al, and Al-O-Al angles, this difference increases with the applied pressure (Figure S15D in the Supporting Information). This is likely because higher

pressure induces a closer packed structure with smaller initial angles. Such smaller, and thus more deformed, initial angles allow for more angular opening and increased ductile deformation during fracture.

To quantitatively understand the role of plasticity mechanisms in intrinsic toughening, we next compare the experimental results with theoretical predictions based on Rouxel's fracture toughness model,<sup>47</sup> in which the absence of plasticity is assumed. For example, in the case of metallic glasses, where plasticity mechanisms are significant, the model predicts lower  $K_{Ic}$  than experimental values.<sup>47</sup> In this approach, fracture toughness is predicted by means of the similarity principle,  $K_{\rm Ic}^{\rm the.} = \sqrt{2\gamma^{\rm t}E'}$  (here  $E' = E/(1-\nu^2)$  for plane strain), where E and  $\nu$  are here taken as the experimental values (Table S2 in the Supporting Information) and  $\gamma^{t}$  is the theoretical fracture surface energy. In turn,  $\gamma^{t}$  is predicted based on the experimental density  $(\rho)$ , the molar mass of the glass, the interatomic bond strength, and the bond concentration along a fracture surface.<sup>47</sup> Here, we first assume that during fracture, the crack propagates through one bond of each oxide unit, i.e., Li-O, Al-O, and B-O bonds, in the  $LiO_x$ , AlO<sub>x</sub>, and BO<sub>x</sub> units, respectively, where x is the number of oxygen atoms connected to the main atom in the structure. We use the diatomic bond energies of 340, 502, and 809 kJ mol<sup>-1</sup> for Li-O, Al-O, and B-O, respectively.<sup>50</sup> With these assumptions, we calculate  $K_{Ic}$ s of all the lithium aluminoborate glasses and find reasonable agreement with experiments (Figure 7 and Table S2 in the Supporting Information). We note that the absolute differences between predicted and experimental  $K_{Ic}$  values become slightly larger with increasing compaction. Notably, for 2 GPa compression, the predicted  $K_{\rm Ic}$  value is 1.09 MPa m<sup>0.5</sup> while the experimental one is 1.36 MPa  $m^{0.5}$ .

This result indeed supports the existence of plasticity in the hot-compressed glass, which is not considered in Rouxel's fracture toughness model, as it only considers the effect of increasing bond density on toughness upon compression. The observed underestimation may arise from the increase of plasticity caused by bond swapping, increasing, and decreasing CNs (Figure 5) of the hot-compressed glasses. The three types of bond changes are inherently related. That is, for a swapping event to occur (see, e.g., Figure 6B), the glass needs to experience both increasing and decreasing CNs. The total decrease of the coordination number of an atom type (Li, Al, or B) during the tensile stress loading (Figure 5A) represents the net number of broken bonds, which, in turn, is the accumulation of bond increase, decrease, and swap of all the atoms of that type. To relate these findings to Rouxel's model, we also increase the number of broken bonds in the theoretical calculation. From Figure 5A, we observe that for 2 GPa compaction, the net number of broken Al-O and B-O bonds increases with ratios of 2.5 and 2.1, respectively, compared to the as-prepared glass, while the number of broken Li-O bonds remains constant. We now assume that the crack propagates through 1.0 bond of Li-O, 2.5 bonds of Al-O, and 2.1 bonds of B-O in the LiOx, AlOx, and BOx units, respectively. This new assumption results in a new predicted K<sub>Ic</sub> value of 1.47 MPa m<sup>0.5</sup>, which is in agreement with the experimental one (1.36 MPa m<sup>0.5</sup>). This suggests that the control of the plasticity mechanism is important for designing damage-tolerant (hard and tough) bulk oxide glasses.

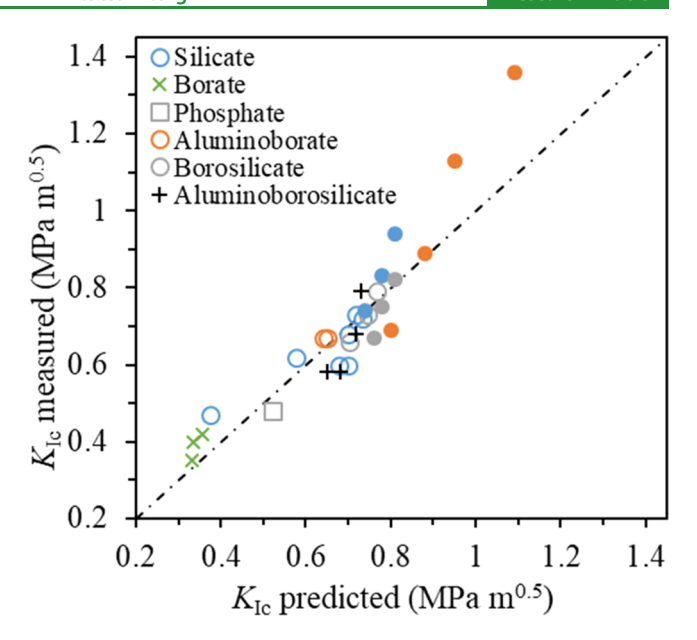


Figure 7. Fracture toughness comparison. Comparison of theoretically predicted and experimental fracture toughness ( $K_{\rm Ic}$ ) values for various oxide glasses. The prediction is explained in the text. Figure is adopted with data from ref 47 with addition of data for silicate and borate glasses<sup>28</sup> and the present as-prepared and compressed glasses. Data are from refs 13, 14, 24, 25, 51–53 and present study for silicate, from ref 47 for borate and phosphate, from ref 51 for aluminosilicate, from refs 24 and 28 and present study for aluminoborate, from refs 13, 14, 24, 25, 28, 47, 51 and this study for borosilicate, and from refs 28 and 51 for aluminoborosilicate. The closed points are data from this study, and the open points are from the literature. The  $K_{\rm Ic}$  data are measured by either single-edge precrack beam, chevron-notched beam (CNB), or chevron-notched short bar (CNSB) methods. Estimated errors for measured  $K_{\rm Ic}$  do not exceed 0.04 MPa m<sup>0.5</sup>.

#### 4. CONCLUSIONS

We have demonstrated that bond switching enables the design of tougher bulk oxide glasses. As shown herein, isostatic N<sub>2</sub>mediated pressure treatment can produce intrinsically denser, stiffer, harder, and tougher glasses. These mechanical properties increase more dramatically for a lithium aluminoborate glass than for soda-lime-silica and sodium borosilicate glasses. Based on MD simulations, the improvement in the mechanical properties of the aluminoborate glass is due to the increase in coordination number changes (both increase and decrease) and bond swapping events during fracture in the densified glasses. These structural transformations enhance plasticity in the compressed glasses and thus increase toughness. In particular, the 2 GPa compressed lithium aluminoborate glass is the toughest bulk oxide glass ever reported (as measured using a self-consistent method), and it also features very high values of hardness and Young's modulus. This glass is a promising candidate for a number of commercial applications due to its chemical<sup>54</sup> and mechanical stability as well as its optical transparency (Figure S2 in the Supporting Information). Compared to commercial Corning Gorilla Glass 4, LiAlB glass compressed at 2 GPa is 16% harder, twice as stiff and tough, but less crack-resistant (~4.5 N for LiAlB at 2 GPa and ~150-600 N for ion exchanged Gorilla Glass).55 It is noteworthy that while crack resistance is a load in the Vickers indentation test that has a 50% crack initiation probability, fracture toughness is the resistance to crack propagation measured by a nonindentation method (SEPB in this study). Of course, we note that the obtained fracture toughness value (1.36 MPa m<sup>0.5</sup>) remains low compared to other material families such as some ductile crystalline and glassy metals, but these lack the main feature of oxide glasses, namely, transparency in the visible region.

The obtained results allow us to summarize the following design principles for enabling bulk oxide glasses that are intrinsically tough: (i) employing oxides with strong covalent bonds, (ii) employing oxides with easily changing CNs such as Al and B, and (iii) enhancing the extent of bond switching (decreasing, increasing, or swapping CN), e.g., by maximizing the concentration of coordination defects in the network. Through the elucidation of the mechanisms needed for intrinsic toughening, we believe that this work paves the way for the design of ultratough oxide glasses.

#### **ASSOCIATED CONTENT**

#### Supporting Information

The Supporting Information is available free of charge at https://pubs.acs.org/doi/10.1021/acsami.1c00435.

> Table with comparison of the results from standard and adapted SEPB setups and adapted SEPB setups as well as a table of experimental, simulated, and predicted results. Figures of X-ray diffraction results, UV-vis transmittance curve of LiAlB glass, final structural relaxation curve of simulated LiAlB at 2 GPa, dependence of the crack-to-box-size-ratio and  $K_{Ic}$  in simulations, curves of comparison of alumina concentration dependence of density, average boron and aluminum coordination numbers between simulation and experiment, comparison between experimental and simulated densities and coordination numbers for LiAlB glasses, stress versus strain curve of simulated fracture in SiO2 glass, obtained  $K_{Ic}$  values for all simulated glasses, stress versus strain curve and brittleness index versus pressure curve for LiAlB glass, average coordination numbers during tension of LiAlB glasses, coordination number distribution of LiAlB glasses, bond switching analysis of simulated NaBSi and SLS glasses, average fractions of bond switching events during tensile deformation of all simulated glasses, visualizations of spatial distribution of bond switching events in LiAlB glasses, and dependence of strain on the average bond-angle curves (PDF)

#### AUTHOR INFORMATION

## **Corresponding Author**

Morten M. Smedskjaer - Department of Chemistry and Bioscience, Aalborg University, Aalborg East 9220, Denmark; orcid.org/0000-0003-0476-2021; Email: mos@bio.aau.dk

## **Authors**

Theany To - Department of Chemistry and Bioscience, Aalborg University, Aalborg East 9220, Denmark Søren S. Sørensen – Department of Chemistry and Bioscience, Aalborg University, Aalborg East 9220, Denmark Johan F. S. Christensen - Department of Chemistry and Bioscience, Aalborg University, Aalborg East 9220, Denmark; o orcid.org/0000-0002-8842-2843 Rasmus Christensen - Department of Chemistry and

Bioscience, Aalborg University, Aalborg East 9220, Denmark

Lars R. Jensen – Department of Materials and Production, Aalborg University, Aalborg East 9220, Denmark

Michal Bockowski - Institute of High-Pressure Physics, Polish Academy of Sciences, Warsaw 0114, Poland

Mathieu Bauchy - Department of Civil and Environmental Engineering, University of California Los Angeles, Los Angeles, California 90095, United States; oorcid.org/ 0000-0003-4600-0631

Complete contact information is available at: https://pubs.acs.org/10.1021/acsami.1c00435

#### **Author Contributions**

M.M.S. conceived the study. T.T., S.S.S., and M.M.S. planned the experiments and simulations. T.T. prepared the samples and M.Bockowski performed the high-pressure treatment. T.T. and L.R.J. performed the mechanical testing. S.S.S., J.F.S.C., and R.C. performed the MD simulations and analyses, with input from M.Bauchy. All authors participated in discussing the data. T.T., S.S.S., J.F.S.C., and M.M.S. wrote the manuscript with revisions from the other authors.

This work was supported by VILLUM FONDEN under research grant no. 13253. M.Bauchy acknowledges funding from the National Science Foundation under grants 1762292 and 1928538. We also thank Aalborg University for access to computational resources through CLAAUDIA.

#### **Notes**

The authors declare no competing financial interest.

#### **REFERENCES**

- (1) Greaves, G. N.; Greer, A. L.; Lakes, R. S.; Rouxel, T. Poisson's Ratio and Modern Materials. Nat. Mater. 2011, 10, 823-837.
- (2) Wondraczek, L.; Mauro, J. C.; Eckert, J.; Kühn, U.; Horbach, J.; Deubener, J.; Rouxel, T. Towards Ultrastrong Glasses. Adv. Mater. 2011, 23, 4578-4586.
- (3) Ritchie, R. O. The Conflicts between Strength and Toughness. Nat. Mater. 2011, 10, 817-822.
- (4) Ritchie, R. O. The Quest for Stronger, Tougher Materials. Science 2008, 320, 448.
- (5) Yu, X.; Marks, T. J.; Facchetti, A. Metal Oxides for Optoelectronic Applications. Nat. Mater. 2016, 15, 383-396.
- (6) Nomura, K.; Ohta, H.; Takagi, A.; Kamiya, T.; Hirano, M.; Hosono, H. Room-Temperature Fabrication of Transparent Flexible Thin-Film Transistors Using Amorphous Oxide Semiconductors. Nature 2004, 432, 488-492.
- (7) Idota, Y.; Kubota, T.; Matsufuji, A.; Maekawa, Y.; Miyasaka, T. Tin-Based Amorphous Oxide: A High-Capacity Lithium-Ion-Storage Material. Science 1997, 276, 1395-1397.
- (8) Januchta, K.; Stepniewska, M.; Jensen, L. R.; Zhang, Y.; Somers, M. A. J.; Bauchy, M.; Yue, Y.; Smedskjaer, M. M. Breaking the Limit of Micro-Ductility in Oxide Glasses. Adv. Sci. 2019, 6, 1901281.
- (9) Januchta, K.; Youngman, R. E.; Goel, A.; Bauchy, M.; Logunov, S. L.; Rzoska, S. J.; Bockowski, M.; Jensen, L. R.; Smedskjaer, M. M. Discovery of Ultra-Crack-Resistant Oxide Glasses with Adaptive Networks. Chem. Mater. 2017, 29, 5865-5876.
- (10) Sglavo, V. M.; Prezzi, A.; Zandonella, T. Engineered Stress-Profile Silicate Glass: High Strength Material Insensitive to Surface Defects and Fatigue. Adv. Eng. Mater. 2004, 6, 344-349.
- (11) Karlsson, S.; Jonson, B.; Stålhandske, C. The Technology of Chemical Glass Strengthening - A Review. Glass Technol. 2010, 51,
- (12) Irwin, G. R. Analysis of Stresses and Strains near the End of a Crack Traversing a Plate. Spie Milest Ser MS 1997, 137, 16.

- (13) Quinn, G. D.; Swab, J. J. Fracture Toughness of Glasses as Measured by the SCF and SEPB Methods. *J. Eur. Ceram. Soc.* **2017**, 37, 4243–4257.
- (14) To, T. Fracture Toughness and Fracture Energy of Inorganic and Non-Metallic Glass. Université de Rennes 1 (PhD thesis), 2019.
- (15) Østergaard, M. B. M. B.; Hansen, S. R.; Januchta, K.; To, T.; Rzoska, S. J. S. J.; Bockowski, M.; Bauchy, M.; Smedskjaer, M. M. M. Revisiting the Dependence of Poisson's Ratio on Liquid Fragility and Atomic Packing Density in Oxide Glasses. *Materials* **2019**, *12*, 2439.
- (16) ASTM. C1421–10, Standard Test Methods for Determination of Fracture Toughness of Advanced Ceramics at Ambient Temperature; ASTM International: West Conshohocken, PA, 2010.
- (17) Luo, J.; Mauro, J. C. Transparent Silicate Glasses with High Fracture Toughness. 10427972, 2019.
- (18) Bauchy, M.; Wang, B.; Wang, M.; Yu, Y.; Abdolhosseini Qomi, M. J.; Smedskjaer, M. M.; Bichara, C.; Ulm, F. J.; Pellenq, R. Fracture Toughness Anomalies: Viewpoint of Topological Constraint Theory. *Acta Mater.* **2016**, *121*, 234–239.
- (19) Yuan, F.; Huang, L. Brittle to Ductile Transition in Densified Silica Glass. Sci. Rep. 2014, 4, 5035.
- (20) Luo, J.; Wang, J.; Bitzek, E.; Huang, J. Y.; Zheng, H.; Tong, L.; Yang, Q.; Li, J.; Mao, S. X. Size-Dependent Brittle-to-Ductile Transition in Silica Glass Nanofibers. *Nano Lett.* **2016**, *16*, 105–113.
- (21) Zheng, K.; Wang, C.; Cheng, Y. Q.; Yue, Y.; Han, X.; Zhang, Z.; Shan, Z.; Mao, S. X.; Ye, M.; Yin, Y.; Ma, E. Electron-Beam-Assisted Superplastic Shaping of Nanoscale Amorphous Silica. *Nat. Commun.* **2010**, *1*, 24.
- (22) Frankberg, E. J.; Kalikka, J.; Ferré, F. G.; Joly-Pottuz, L.; Salminen, T.; Hintikka, J.; Hokka, M.; Koneti, S.; Douillard, T.; Le Saint, B.; Kreiml, P.; Cordill, M. J.; Epicier, T.; Stauffer, D.; Vanazzi, M.; Roiban, L.; Akola, J.; Di Fonzo, F.; Levänen, E.; Masenelli-Varlot, K. Highly Ductile Amorphous Oxide at Room Temperature and High Strain Rate. *Science* 2019, 366, 864–869.
- (23) Rouxel, T.; Yoshida, S. The Fracture Toughness of Inorganic Glasses. J. Am. Ceram. Soc. 2017, 100, 4374-4396.
- (24) To, T.; Jensen, L. R.; Smedskjaer, M. M. On the Relation between Fracture Toughness and Crack Resistance in Oxide Glasses. *J. Non-Cryst. Solids* **2020**, *534*, 119946.
- (25) To, T.; Célarié, F.; Roux-Langlois, C.; Bazin, A.; Gueguen, Y.; Orain, H.; Le Fur, M.; Burgaud, V.; Rouxel, T. Fracture Toughness, Fracture Energy and Slow Crack Growth of Glass as Investigated by the Single-Edge Precracked Beam (SEPB) and Chevron-Notched Beam (CNB) Methods. *Acta Mater.* **2018**, *146*, 1–11.
- (26) To, T.; Sørensen, S. S.; Stepniewska, M.; Qiao, A.; Jensen, L. R.; Bauchy, M.; Yue, Y.; Smedskjaer, M. M. Fracture Toughness of a Metal-Organic Framework Glass. *Nat. Commun.* **2020**, *11*, 2593.
- (27) Smedskjaer, M. M.; Rzoska, S. J.; Bockowski, M.; Mauro, J. C. Mixed Alkaline Earth Effect in the Compressibility of Aluminosilicate Glasses. *J. Chem. Phys.* **2014**, *140*, No. 054511.
- (28) Januchta, K.; To, T.; Bødker, M. S.; Rouxel, T.; Smedskjaer, M. M. Elasticity, Hardness, and Fracture Toughness of Sodium Aluminoborosilicate Glasses. *J. Am. Ceram. Soc.* **2019**, *102*, 4520–4537.
- (29) To, T.; Stabler, C.; Ionescu, E.; Riedel, R.; Célarié, F.; Rouxel, T. Elastic Properties and Fracture Toughness of SiOC-Based Glass-Ceramic Nanocomposites. *J. Am. Ceram. Soc.* **2020**, *103*, 491–499.
- (30) Srawley, J. E. Wide Range Stress Intensity Factor Expressions for ASTM E 399 Standard Fracture Toughness Specimens. *Int. J. Fract.* **1976**, 12, 475–476.
- (31) Brown, W. M.; Wang, P.; Plimpton, S. J.; Tharrington, A. N. Implementing Molecular Dynamics on Hybrid High Performance Computers Short Range Forces. *Comput. Phys. Commun.* **2011**, *182*, 898–911.
- (32) Plimpton, S. Fast Parallel Algorithms for Short-Range Molecular Dynamics. *J. Comput. Phys.* **1995**, *117*, 1–19.
- (33) Sundararaman, S.; Huang, L.; Ispas, S.; Kob, W. New Interaction Potentials for Borate Glasses with Mixed Network Formers. *J. Chem. Phys.* **2020**, *152*, 104501.

- (34) Shih, Y.-T.; Sundararaman, S.; Ispas, S.; Huang, L. New Interaction Potentials for Alkaline Earth Silicate and Borate Glasses. arXiv Prepr. arXiv2102.08733 2021.
- (35) Gersten, J. I.; Smith, F. W. The Physics and Chemistry of Materials; Wiley, 2001.
- (36) Brochard, L.; Hantal, G.; Laubie, H.; Ulm, F. J.; Pellenq, R. J.-M. Fracture Mechanisms in Organic-Rich Shales: Role of Kerogen. *Poromechanics V* **2013**, *5*, 2471–2480.
- (37) Wang, B.; Yu, Y.; Lee, Y. J.; Bauchy, M. Intrinsic Nano-Ductility of Glasses: The Critical Role of Composition. *Front. Mater.* **2015**, *2*, 11.
- (38) Brochard, L.; Hantal, G.; Laubie, H.; Ulm, F. J.; Pellenq, R. J. M. Capturing Material Toughness by Molecular Simulation: Accounting for Large Yielding Effects and Limits. *Int. J. Fract.* **2015**, 194, 149–167.
- (39) Swiler, T. P.; Simmons, J. H.; Wright, A. C. Molecular Dynamics Study of Brittle Fracture in Silica Glass and Cristobalite. *J. Non-Cryst. Solids* **1995**, *182*, 68–77.
- (40) Pedone, A.; Malavasi, G.; Cristina Menziani, M.; Segre, U.; Cormack, A. N. Molecular Dynamics Studies of Stress-Strain Behavior of Silica Glass under a Tensile Load. *Chem. Mater.* **2008**, *20*, 4356–4366.
- (41) Zhang, Z.; Ispas, S.; Kob, W. The Critical Role of the Interaction Potential and Simulation Protocol for the Structural and Mechanical Properties of Sodosilicate Glasses. *J. Non-Cryst. Solids* **2020**, 532, 119895.
- (42) Urata, S.; Ando, R.; Ono, M.; Hayashi, Y. Molecular Dynamics Study on Nano-Particles Reinforced Oxide Glass. *J. Am. Ceram. Soc.* **2018**, *101*, 2266–2276.
- (43) Wang, B.; Yu, Y.; Wang, M.; Mauro, J. C.; Bauchy, M. Nanoductility in Silicate Glasses Is Driven by Topological Heterogeneity. *Phys. Rev. B* **2016**, *93*, No. 064202.
- (44) Januchta, K.; Youngman, R. E.; Goel, A.; Bauchy, M.; Rzoska, S. J.; Bockowski, M.; Smedskjaer, M. M. Structural Origin of High Crack Resistance in Sodium Aluminoborate Glasses. *J. Non-Cryst. Solids* **2017**, *460*, 54–65.
- (45) Svenson, M. N.; Guerette, M.; Huang, L.; Lönnroth, N.; Mauro, J. C.; Rzoska, S. J.; Bockowski, M.; Smedskjaer, M. M. Universal Behavior of Changes in Elastic Moduli of Hot Compressed Oxide Glasses. *Chem. Phys. Lett.* **2016**, *651*, 88–91.
- (46) Kapoor, S.; Wondraczek, L.; Smedskjaer, M. M. Pressure-Induced Densification of Oxide Glasses at the Glass Transition. *Front. Mater.* **2017**, *4*, 1.
- (47) Rouxel, T. Fracture Surface Energy and Toughness of Inorganic Glasses. Scr. Mater. **2017**, 137, 109–113.
- (48) Fernandes, H. R.; Kapoor, S.; Patel, Y.; Ngai, K.; Levin, K.; Germanov, Y.; Krishtopa, L.; Kroeker, S.; Goel, A. Composition-Structure-Property Relationships in Li<sub>2</sub>O-Al<sub>2</sub>O<sub>3</sub>-B<sub>2</sub>O<sub>3</sub> Glasses. *J. Non-Cryst. Solids* **2018**, 502, 142–151.
- (49) Evans, A. G. Perspective on the Development of High-Toughness Ceramics. J. Am. Ceram. Soc. 1990, 73, 187–206.
- (50) Luo, Y.-R. Handbook of Bond Dissociation Energies in Organic Compounds; CRC press, 2002, DOI: 10.1201/9781420039863.
- (51) Kato, Y.; Yamazaki, H.; Yoshida, S.; Matsuoka, J. Effect of Densification on Crack Initiation under Vickers Indentation Test. *J. Non-Cryst. Solids* **2010**, *356*, 1768–1773.
- (52) Scannell, G.; Huang, L.; Rouxel, T. Elastic Properties and Indentation Cracking Behavior of Na<sub>2</sub>O-TiO<sub>2</sub>-SiO<sub>2</sub> Glasses. *J. Non-Cryst. Solids* **2015**, 429, 129–142.
- (53) Scannell, G.; Laille, D.; Huang, L.; Rouxel, T. Interaction between Deformation and Crack Initiation under Vickers Indentation in Na<sub>2</sub>O-TiO<sub>2</sub>-SiO<sub>2</sub> Glasses. *Front. Mater.* **2017**, *4*, 6.
- (54) Mascaraque, N.; Frederiksen, K. F.; Januchta, K.; Youngman, R. E.; Bauchy, M.; Smedskjaer, M. M. Competitive Effects of Modifier Charge and Size on Mechanical and Chemical Resistance of Aluminoborate Glasses. *J. Non-Cryst. Solids* **2018**, 499, 264–271.
- (55) Corning® Gorilla® Glass 4 Product Information Sheet, Corning Incorporated (2015).